




Accounting for Numerical-Relativity Calibration Uncertainty in Gravitational-Wave Modeling and Inference

Lorenzo Pompili ¹, Alessandra Buonanno ^{1,2} and Michael Pürrer ^{3,4,1}

¹Max Planck Institute for Gravitational Physics (Albert Einstein Institute), Am Mühlenberg 1, Potsdam 14476, Germany

²Department of Physics, University of Maryland, College Park, MD 20742, USA

³Department of Physics, East Hall, University of Rhode Island, Kingston, RI 02881, USA

⁴Center for Computational Research, Tyler Hall, University of Rhode Island, Kingston, RI 02881, USA

(Dated: October 23, 2024)

The increasing sensitivity of current and upcoming gravitational-wave (GW) detectors poses stringent requirements on the accuracy of the GW models used for data analysis. If these requirements are not met, systematic errors could dominate over statistical uncertainties, hindering our ability to extract astrophysical and cosmological information, and conduct precise tests of General Relativity. In this work, we present a novel method to mitigate waveform-systematic errors, by incorporating and marginalizing over waveform-uncertainty estimates, which are modeled as probability distributions for the numerical-relativity calibration parameters of effective-one-body waveform models. By analyzing simulated GW signals of loud “golden” binary–black-hole systems, we show that our method significantly reduces biases in the recovered parameters, highlighting its potential to improve the robustness of GW parameter estimation with upcoming observing runs and next-generation ground-based facilities, such as the Einstein Telescope and Cosmic Explorer.

Introduction— Gravitational-wave (GW) astronomy has rapidly advanced since the first GW observation from a binary–black-hole (BBH) merger [1], with about 100 compact-binary signals detected by the LIGO-Virgo-KAGRA (LVK) collaboration [2–5] and by independent analyses [6, 7]. These observations have shed light on the mass and spin distributions of BHs and neutron stars (NSs) [8], improved constraints on the nuclear equation of state of NSs [9], obtained independent measurements of cosmological parameters [10, 11], and enabled tests of General Relativity (GR) in the highly dynamical and strong-field regime [12, 13].

Advancements in gravitational waveform modeling (e.g., see [14–31]) have been crucial to the success of this endeavor, with waveform models being sufficiently accurate to analyze most detected signals [32, 33], with only a few exceptions where different models recovered noticeably different parameters [5, 34, 35]. Next-generation (XG) GW detectors on the ground, such as the Einstein Telescope (ET) [36] and Cosmic Explorer (CE) [37], and the space-based LISA [38], will offer unprecedented sensitivity, with signal-to-noise ratios (SNR) up to two orders of magnitude higher than current detectors [39]. This increased sensitivity makes waveform accuracy increasingly critical, as statistical uncertainties approach the systematic biases of the GW approximant models. Several studies predict severe biases in parameter estimation (PE) due to mismodeling errors with the upcoming fifth LVK observational run (O5) and XG detectors [29, 33, 40–44], and the risk of false GR deviations [45–48]. Even numerical-relativity (NR) simulations [49–51], the benchmark for generating highly accurate waveforms, are expected to fall short of the required accuracy [52, 53].

Waveform models for compact binaries combine analytical and NR results. The effective-one-body (EOB) approach [54–58] synthesizes and resums analytical information from various perturbative methods for solving Einstein’s equations, with current EOB waveform models primarily relying on re-

summations of the post-Newtonian (PN) [59, 60] expansion, applicable in the weak-field and small-velocity limit. To improve agreement with NR simulations, higher-order PN coefficients, which are currently unknown, are often calibrated using NR data (e.g., see [15, 19, 21, 27, 28, 61]).

A possible way to improve waveform accuracy is to include higher-order analytical information, while pushing calibration parameters to even higher orders. However, this requires careful studies on how to incorporate and resum this information (e.g., see [27, 28, 62–64]), and improvements in the strong-field regime are not always guaranteed. Leveraging novel perturbative methods, such as the gravitational self-force (GSF) [65–69] and the post-Minkowskian (PM) [70–76] approximations, offers another promising avenue. Finally, improving the NR calibration of waveform models by employing longer, higher-resolution simulations covering more of the parameter space is crucial [19, 77].

A common approach to address waveform systematics is to combine predictions from different waveform models. This can be done either by mixing posterior samples from various approximants [5, 32, 78, 79], or by sampling over a set of models treated as hyperparameters in the analysis [80–83]. However, if none of the models employed is accurate enough, these methods are not guaranteed to avoid biases in the inferred parameter estimates. A complementary approach to avoid biased inference involves integrating error estimates directly into waveform models. Proposed methods include using Gaussian process regression (GPR) to interpolate either waveform residuals or directly NR waveforms [84–90], using frequency-dependent amplitude and phase corrections, as in the case of detector-calibration uncertainty [91, 92], or introducing additional higher-order parameters designed to capture currently unknown PN terms [42]. Similar methods have also been applied to model the post-merger phase of NS coalescences [93, 94], as well as in kilonova modeling and inference [95]. In these approaches, waveform modeling uncer-

tainties are accounted for by marginalizing over these additional degrees of freedom during the inference process. While this may lead to less precise parameter estimates (e.g., wider posterior distributions), it should improve their robustness, ensuring they remain reliable even in the presence of systematic modeling errors.

Nonetheless, most studies attempting to incorporate error estimates into waveform models often involved simplified physical descriptions (e.g., non-spinning binaries [42, 90]), and did not assess the impact of this approach on the analysis of realistic signals that could be observed with upcoming runs and XG detectors. In this study, we address this gap. As proof of principle, we employ a state-of-the-art quasi-circular aligned-spin multipolar EOB model SEOBNRv5HM [28, 63, 69, 96], and analyze synthetic signals from NR surrogate waveforms, hybridized to PN-EOB ones (NRHybSur3dq8 [97]), for loud “golden” BBH systems at SNRs consistent with current and future observations, using full Bayesian inference.

Similarly to Refs. [87, 90], we propose a semi-parametric probabilistic model for the GW signal from a BBH, which not only provides a best-fit point estimate but also allows for drawing waveform samples. We do so by modeling posterior probability distributions of the model’s NR-calibration parameters, obtained from 441 NR simulations of aligned-spin BBHs produced with the Spectral Einstein code of the Simulating eXtreme Spacetimes (SXS) Collaboration [19, 22, 97–109], and one produced with the Einstein Toolkit [110]. We interpolate the probability distributions across parameter space using mixture density networks (MDNs) [111], a neural-network architecture suited for modeling and predicting probability distributions over continuous variables. Using these probability distributions as priors, we sample the NR-calibration parameters together with the standard source parameters during inference, effectively marginalizing over the NR-calibration uncertainty in the model.

SEOBNRv5HM waveform model– We use geometric units $G = 1 = c$, and set $M = m_1 + m_2$ and $\nu = m_1 m_2 / M^2$, where m_1 and m_2 are the BH’s masses. In the EOB formalism, the binary’s conservative dynamics is described by the EOB Hamiltonian $H_{\text{EOB}} = M \sqrt{1 + 2\nu(\hat{H}_{\text{eff}} - 1)}$, where $\hat{H}_{\text{eff}} \equiv H_{\text{eff}}/(\nu M)$ is the specific Hamiltonian of an effective test-body of reduced mass νM moving in the (deformed) Kerr spacetime, being $0 \leq \nu \leq 1/4$ the deformation parameter. We also introduce the mass ratio $q = m_1/m_2 > 1$. We limit to aligned spins and introduce the combinations $\chi_{\text{eff}} = (m_1\chi_1 + m_2\chi_2)/M$ and $\chi_a = (m_1\chi_1 - m_2\chi_2)/M$.

The gravitational polarizations can be written as $h_+ - ih_\times = \sum_{\ell, m} {}_{-2}Y_{\ell m}(\varphi, \iota) h_{\ell m}(t)$, where ${}_{-2}Y_{\ell m}(\varphi, \iota)$ are the -2 spin-weighted spherical harmonics, with φ and ι being the azimuthal and polar angles to the observer. The inspiral-merger-ringdown (ℓ, m) modes are given by $h_{\ell m} = h_{\ell m}^{\text{insp-plunge}} \vartheta(t_{\text{peak}}^{22} - t) + h_{\ell m}^{\text{merg-RD}} \vartheta(t - t_{\text{peak}}^{22})$, where ϑ is the Heaviside step function and t_{peak}^{22} is the peak time of the $(2, 2)$ -mode amplitude. The inspiral-plunge modes are based on a factorization of the PN GW modes [15, 112–114], evaluated on the dynamics ob-

tained from the EOB equations of motion [55, 115]. For the merger-ringdown part of the waveform, we use a phenomenological ansatz [19, 28, 116–118], informed by NR and BH perturbation theory.

The accuracy of EOB waveforms is improved through calibration to NR simulations. For the inspiral-plunge stage, this is achieved by introducing higher-order PN terms in the EOB Hamiltonian, whose coefficients are tuned to NR, and fitting the merger time (i.e., t_{peak}^{22}) to NR. The SEOBNRv5HM model [28] employs three calibration parameters $\theta \equiv (\Delta t_{\text{NR}}, a_6, d_{\text{SO}})$. Here, Δt_{NR} is defined by $t_{\text{peak}}^{22} = t_{\text{ISCO}} + \Delta t_{\text{NR}}$, where t_{ISCO} is the time at which $r = r_{\text{ISCO}}$, with r_{ISCO} the radius of the Kerr ISCO [119] with the mass and spin of the remnant BH [120, 121]. The parameter a_6 is a 5PN non-spinning coefficient and d_{SO} is a 4.5PN spin-orbit coefficient in H_{EOB} . The SEOBNRv5HM model is calibrated to 442 aligned-spin NR waveforms covering mass ratios q from 1 to 20 in the non-spinning limit, and spins ranging from $-0.998 \leq \chi_i \leq 0.998$ for $q = 1$ to $-0.5 \leq \chi_1 \leq 0.5$, $\chi_2 = 0$ for $q = 15$ (see Fig. 2 in Ref. [28]). In this work, we focus on the inspiral-merger calibration parameters, as they have the largest impact on most signals, except those dominated by the ringdown stage. By modifying the orbital dynamics, these parameters provide a coherent correction to all waveform modes. Additionally, we focus on the spin sector since the non-spinning sector shows significantly higher accuracy [28]. Thus, we consider $\theta = (\Delta t_{\text{NR}}, d_{\text{SO}})$.

Probabilistic waveform model– Waveform accuracy is often quantified by of the mismatch \mathcal{M} (or unfaithfulness), defined as 1 minus the overlap between the normalized waveforms, maximized over a relative time and phase shift:

$$\mathcal{M} = 1 - \max_{\varphi_0, t_0} \frac{(h_1 | h_2)}{\sqrt{(h_1 | h_1)(h_2 | h_2)}}. \quad (1)$$

The overlap is a noise-weighted inner product [122, 123] $(h_1 | h_2) \equiv 4 \text{Re} \int_{f_1}^{f_2} df \tilde{h}_1(f) \tilde{h}_2^*(f) / S_n(f)$, where $\tilde{h}(f)$ is the Fourier transform of the time-domain signal, the $*$ superscript indicates complex conjugation, and $S_n(f)$ is the power spectral density (PSD) of the detector noise. The optimal SNR of a signal h is $\text{SNR} = \sqrt{(h | h)}$.

The SEOBNRv5HM calibration procedure is outlined in Refs. [19, 28]. It essentially consists of determining values of the calibration parameters θ that minimize a combination of the mismatch and the difference in merger time δt_{merger} (defined as the peak of the $(2, 2)$ -mode amplitude) between EOB and NR waveforms with the same physical parameters $\Lambda \equiv (q, \chi_1, \chi_2)$. This is carried out in a Bayesian fashion using the Bilby [124] package, and the pySEOBNR code [96]. One defines a likelihood function of the form

$$p(\Lambda^{\text{NR}} | \theta) \propto \exp \left[-\frac{1}{2} \left(\frac{\mathcal{M}_{\text{max}}(\theta)}{\sigma_{\mathcal{M}}} \right)^2 - \frac{1}{2} \left(\frac{\delta t_{\text{merger}}(\theta)}{\sigma_t} \right)^2 \right], \quad (2)$$

where $\mathcal{M}_{\text{max}}(\theta)$ is the maximum $(2, 2)$ -mode mismatch between EOB and NR waveforms over the total mass range $10M \leq M_{\odot} \leq 200M$. $\sigma_{\mathcal{M}}$ is chosen to be 10^{-3} , and $\sigma_t = 5M$,

these being conservative estimates of NR errors [28, 98]. A posterior distribution $p(\boldsymbol{\theta} | \Lambda)$ is obtained for each NR configuration with parameters Λ using nested sampling [125, 126], assuming uniform priors on $\boldsymbol{\theta}$. After a post-processing step to select only one mode of each calibration posterior, in SEOBNRv5HM one fits a point measure $\boldsymbol{\theta}(\Lambda)$ for each NR simulation, like the median of the distribution, over the Λ parameter space, using least-square hierarchical fits. We use the final calibration posteriors from Ref. [28].

In this work, we fit the *full* posterior distributions of the calibration parameters $p(\boldsymbol{\theta} | \Lambda)$, instead of point estimates $\boldsymbol{\theta}(\Lambda)$. This provides a “best-fit” point measure from, e.g., the mean of the posterior, while also giving access to parameter uncertainty. It can be interpreted as a probabilistic waveform model [87, 88, 90] by drawing samples of the calibration parameters. We model the calibration posteriors $p(\boldsymbol{\theta} | \Lambda)$ as a mixture of Gaussians depending on physical parameters, using MDNs. MDNs offer a versatile alternative to standard, single-output, GPR approaches [90], allowing for the modeling of not only the uncertainty in individual parameters, but also the correlations between different NR-calibration parameters. We define $p(\boldsymbol{\theta} | \Lambda) \approx \sum_{k=1}^K \pi_k(\Lambda) \mathcal{N}(\boldsymbol{\theta} | \mu_k(\Lambda), \Sigma_k(\Lambda))$, where $\mathcal{N}(\boldsymbol{\theta} | \mu, \Sigma)$ are multivariate Gaussian distributions with mean μ and covariance matrix Σ , e.g., $\mathcal{N}(\boldsymbol{\theta} | \mu, \Sigma) \propto \exp\left[-\frac{1}{2}(\boldsymbol{\theta} - \mu)^T \Sigma^{-1}(\boldsymbol{\theta} - \mu)\right]$, and $\pi_k(\Lambda)$ are the weights of the K Gaussians in the mixture. The weights, means and covariance matrices are modeled with neural networks using the PyTorch framework [127].

To improve the extrapolation behavior of the model, we fit the residuals after subtracting the least-square fits of Ref. [28], which we denote $\delta\boldsymbol{\theta} = (\delta\Delta t_{\text{NR}}, \delta d_{\text{SO}})$. Specifically, we train the MDN to model the NR-calibration posterior residuals, denoted as $p(\delta\boldsymbol{\theta} | \Lambda)$. Details on the neural network architecture and the sanity checks that we performed are provided in the Supplemental Material. Figure 1 shows an SEOBNRv5HM waveform with its uncertainty estimate, from different calibration posterior samples, for $\Lambda \equiv (q, \chi_1, \chi_2) = (3.0, 0.45, 0.45)$, compared against the NRHybSur3dq8 model.

We marginalize over modeling uncertainties in PE by sampling both the source parameters and corrections to the NR-calibration parameters $\delta\boldsymbol{\theta}$, using $p(\delta\boldsymbol{\theta} | \Lambda)$ as conditional priors. As in Ref. [42] we also compare these results to those obtained using uniform priors on $\delta\boldsymbol{\theta}$. We choose a range within $[-50, 50]$ for both $\delta\Delta t_{\text{NR}}$ and δd_{SO} , slightly broader than the typical range of NR-calibration posteriors.

Results – We now assess the impact of marginalizing over the NR-calibration uncertainty in the parameter inference of loud “golden” BBH systems. The GW strain of quasi-circular, aligned-spin BBHs is characterized by 11 parameters $\boldsymbol{\lambda} = \{\mathcal{M}_c, 1/q, \chi_1, \chi_2, d_L, \alpha, \delta, \iota, \varphi, \psi, t_c\}$. We parameterize the masses in terms of the chirp mass $\mathcal{M}_c = (m_1 m_2)^{3/5} / M^{1/5}$ and inverse mass ratio $1/q$. The position of the binary is described by its luminosity distance, d_L , and the coordinates on the plane of the sky, (α, δ) . The orientation of the binary is described by the polar angle, ι , and the azimuthal angle, φ , to the observer in the source frame [128] at the reference frequency, which

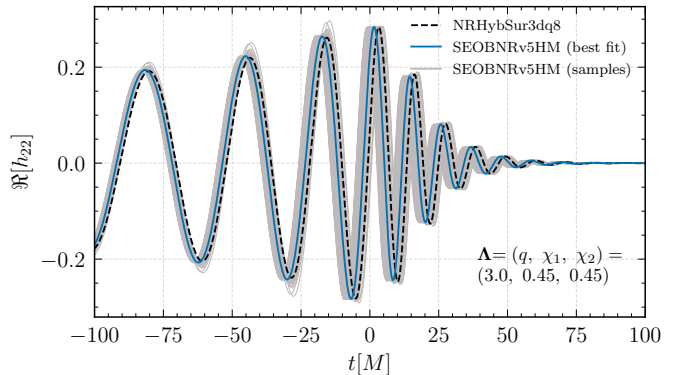


Figure 1. An SEOBNRv5HM waveform with its uncertainty estimate, compared against the NRHybSur3dq8 model after a low-frequency alignment. The waveforms start at a frequency of 20 Hz for a binary with total mass $M = 60 M_\odot$. The best-fit SEOBNRv5HM waveform uses as NR-calibration parameters $\boldsymbol{\theta}$ the mean of the MDN fit of the calibration posterior $p(\boldsymbol{\theta} | \Lambda)$, while the uncertainty corresponds to 100 samples from the same distribution. The time $t = 0$ corresponds to the peak of the (2, 2) mode of the NR waveform.

we always set to $f_{\text{ref}} = 20$ Hz. Finally, the relative contribution of the two gravitational polarizations, $h_+(t)$ and $h_\times(t)$, is described by the polarization angle, ψ , while the reference for the time is given by the coalescence time, t_c .

To simulate and analyze the GW signals we use the parallel Bilby package [124, 129, 130] and the nested sampler Dynesty [131]. We employ standard priors for all the parameters [130]. We consider four detector network configurations: a O4 network (corresponding to the current fourth observing run) with two advanced LIGO at O4 sensitivity [132] and one advanced Virgo detector at design sensitivity [133]; two upgraded LIGO networks with O5 and A# sensitivities [134] alongside advanced Virgo; and one ET-A# network with LIGO detectors at A# sensitivities combined with a 10 km ET at Virgo. The low-frequency cutoff varies across these networks: 20 Hz for O4, 15 Hz for O5, 10 Hz for the A# and the ET-A# network [135].

For each detector network, we simulate two BBH signals in zero-noise using the NRHybSur3dq8 model, selecting configurations with unequal masses ($q = 3$) and either positive ($\chi_1 = \chi_2 = 0.45$) or negative ($\chi_1 = \chi_2 = -0.45$) spins. These configurations fall within the model’s NR-calibration region but are still relatively challenging, so mismodeling errors may be significant at high SNR. We set the detector-frame total mass of the binary to $M = 60 M_\odot$, which gives $\mathcal{M}_c \approx 21.976$ for $q = 3$. Common parameters for both systems include: inclination angle $\iota = 0.438$, reference phase $\varphi = 0$, sky location $\alpha = 1.827$, $\delta = -1.252$ (radians), luminosity distance $d_L = 600.0 \text{ Mpc}$, polarization angle $\psi = 2.562$ and GPS time at the geocenter 1126259462.409 s. For the negative (positive)-spin configuration, the network optimal SNR ranges from 39.27 (51.75) in the O4 network, to 366.72 (439.23) in the ET-A# network.

For each of the 8 configurations, we perform three recoveries. In the first, we use the default SEOBNRv5HM model and

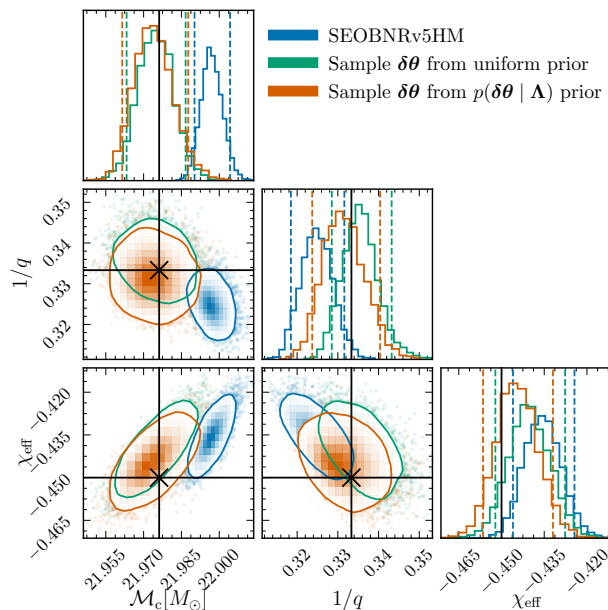


Figure 2. Marginalized posterior distributions for the chirp mass, inverse mass ratio, and effective spin in the ET-A# detector network. Parameter estimation is performed by injecting a NRHybSur3dq8 signal, with an SNR of 366.72, and recovering it using three versions of SEOBNRv5HM: one sampling only the standard source parameters, and the others including corrections to the NR-calibration parameters $\delta\theta$. For $\delta\theta$, both uniform priors and $p(\delta\theta | \Lambda)$ priors, reflecting NR-calibration uncertainty, are used. In the latter case, we accurately recover the injected values within the 90% credible region, indicated by dashed vertical lines in the 1D marginalized posteriors and contours in the 2D marginalized posteriors.

sample only the standard source parameters. In the other two, we account for NR-calibration uncertainty by sampling over corrections to the NR-calibration parameters $\delta\theta$ with either $p(\delta\theta | \Lambda)$ or uniform priors, as previously described.

Figure 2 shows marginalized posterior distributions for the chirp mass, inverse mass ratio, and effective spin, for the negative-spin configuration in the ET-A# detector network (SNR= 366.72). The SEOBNRv5HM recovery shows biases in M_c , $1/q$, χ_{eff} , with the injected value falling outside of the 90% credible region, indicated by dashed vertical lines in the 1D marginalized posteriors and contours in the 2D marginalized posteriors. Sampling over $\delta\theta$ with uniform priors mitigates these biases, bringing the injected parameters at the edge of the 90% contours. This improvement is partially due to the increase in statistical error, though all parameters also peak closer to the injected values. Using $p(\delta\theta | \Lambda)$ priors for $\delta\theta$ further improves the recovery of $1/q$ and χ_{eff} , with the injected values now falling well within the 2D posteriors. The increase in statistical error and decrease in systematic error when accounting for waveform uncertainties is qualitatively consistent with the earlier results of Refs. [84–86] and with the PN model of Ref. [42]. Biases arise because the template model can provide a better fit to the signal when the parameters are not the true ones. By improving the match through adjustments in “nuisance” parameters like $\delta\theta$, the need for

shifts in the physical parameters is reduced. The increase in statistical error is due to additional correlations introduced by the nuisance parameters.

The left panel of Fig. 3 show the ratio of systematic bias to statistical errors ($\delta\lambda/\Delta\lambda$) for the same set of parameters, as well as inclination and luminosity distance, as a function of the SNR across the four detector networks. We focus on the negative-spin configuration, and discuss the positive-spin one in the Supplemental Material. We take $\delta\lambda$ to be the difference between the injected parameters and the median of the 1D marginalized posteriors, and $\Delta\lambda$ to be half of the width of the 90% 1D credible interval. At SNRs of ~ 100 and higher, the original model exhibits biases in masses and spins (e.g., $|\delta\lambda/\Delta\lambda| > 1$) which are substantially mitigated when accounting for NR-calibration uncertainties, with all cases having $|\delta\lambda/\Delta\lambda| \lesssim 1$ when including corrections to the NR-calibration parameters $\delta\theta$. To understand how much the reduction of $|\delta\lambda/\Delta\lambda|$ is due to an increase in statistical errors, we show in the bottom panel the ratio of $\Delta\lambda$ with and without $\delta\theta$ corrections. For both prior choices, there is an increase of a factor of a few in statistical errors, mainly for masses and spins, with a marginal increase for distance and inclination. MDN-informed priors lead to a smaller increase in statistical errors, especially at lower SNRs where the default SEOBNRv5HM model is unbiased. The increase in statistical error can be below the $\delta\lambda/\Delta\lambda$ ratio of the default SEOBNRv5HM model, even when models with uncertainty corrections achieve $\delta\lambda/\Delta\lambda \lesssim 1$, indicating a shift of the recovered parameters toward the injected values.

To assess the effectiveness of our method across parameter space, we also explore a larger set of 12 configurations with mass ratios $q \in [1.5, 3.0, 6.0]$ and equal spins $\chi_i \in [-0.75, -0.45, 0.45, 0.75]$, fixing the chirp mass to $M_c \simeq 21.976$. For simplicity, we limit our analysis to the A# detector network. At a fixed luminosity distance, the SNR of the injected signal decreases with increasing mass ratio and increases with higher spins, ranging from 88.0 for the configuration with $q = 6$ and $\chi_i = -0.75$, to 187.8 for $q = 1.5$ and $\chi_i = 0.75$. In this case, we recover NRHybSur3dq8 signals using SEOBNRv5HM, either sampling only the standard source parameters, or including corrections to the NR-calibration parameters $\delta\theta$ with $p(\delta\theta | \Lambda)$ priors. The right panels of Fig. 3 show the ratio of systematic bias to statistical errors ($|\delta\lambda/\Delta\lambda|$) across the parameter space, for the chirp mass and χ_{eff} . The left column presents the default SEOBNRv5HM recovery, while the right column shows results sampling on corrections to the NR-calibration parameters $\delta\theta$ with $p(\delta\theta | \Lambda)$ priors. Including corrections to the NR-calibration parameters generally reduces biases across the parameter space, especially for the most challenging configurations with large positive spins and unequal mass ratios.

While biases are generally reduced, they are not always completely eliminated. When considering an approximate model $H(\Lambda)$ and the “true” waveform $h_{\text{true}}(\Lambda)$, we only have an approximate relation $h_{\text{true}}(\Lambda) \simeq H(\Lambda, \theta(\Lambda) + \delta\theta(\Lambda))$. The effectiveness of the $\delta\theta$ correction in reducing the difference

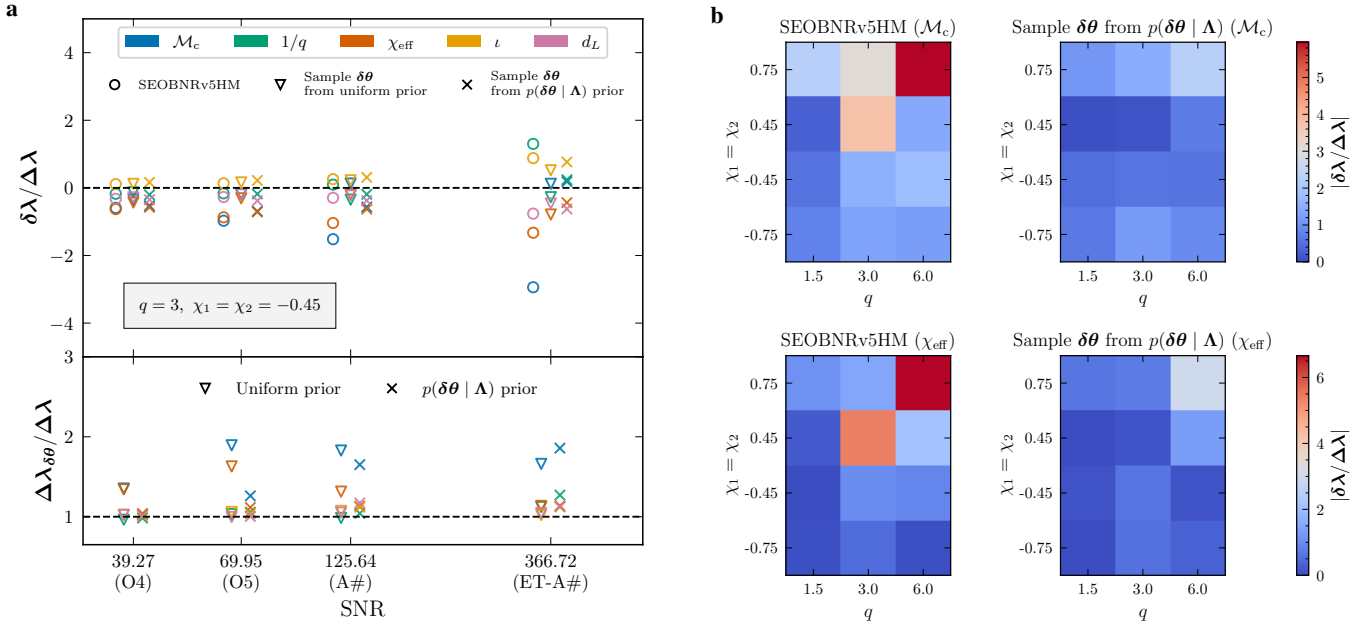


Figure 3. (a) *Top*: Ratio of systematic bias to statistical errors ($\delta\lambda/\Delta\lambda$) for the chirp mass, inverse mass ratio, effective spin, inclination, and luminosity distance, as a function of the network SNR, for upcoming runs, O4, O5, A#, and next-generation ground-based detector networks (ET-A#). Parameter estimation is performed by injecting a NRHybSur3dq8 signal, and recovering it with three versions of SEOBNRv5HM: one sampling only the standard parameters, and the others including corrections to the NR-calibration parameters $\delta\theta$. For $\delta\theta$, both uniform priors and $p(\delta\theta|\Lambda)$ priors, reflecting NR-calibration uncertainty, are used. *Bottom*: Ratio of statistical errors ($\Delta\lambda$) with and without corrections to the NR-calibration parameters $\delta\theta$, using different priors. (b) Ratio of systematic bias to statistical errors ($|\delta\lambda/\Delta\lambda|$) across parameter space, for the chirp mass (*top row*), and effective spin (*bottom row*), in the A# detector network.

between the approximate and “true” waveforms depends crucially on the choice of the calibration parameter θ . Additional corrections, such as higher-order terms in the EOB Hamiltonian and energy flux, or corrections to higher modes, may be relevant depending on the source’s properties and SNR. The $\delta\theta$ corrections we focus on account for the inevitable errors in the fits to NR, as well as the fact that NR is only an approximation of the “true” signal. While this may represent only a partial source of error, it is inherently linked to the construction of all inspiral-merger-ringdown models calibrated to NR, and must be accounted for.

Despite adding extra parameters, the computational cost of recoveries including $\delta\theta$ is lower than for the default model, due to fewer likelihood evaluations needed for convergence. This is especially true with MDN-based priors on $\delta\theta$, with $\sim 30\%$ fewer likelihood evaluations required.

Conclusions— In this work, we introduced a method to mitigate waveform systematic errors, by incorporating and marginalizing over waveform uncertainty estimates. We modeled the latter as probability distributions for the SEOBNRv5HM [28] NR-calibration parameters using MDNs. We demonstrated its effectiveness in significantly reducing systematic errors in the parameter inference of loud “golden” BBH systems observed with upcoming and XG detectors, at the cost of a slight increase in statistical uncertainty.

This method addresses uncertainties within the NR-calibration region of the model, but does not necessarily lead to increasing error estimates in regions of the parameter space lacking training data. However, model differences can be

large outside their NR-calibration region [43]. To account for these extrapolation uncertainties, one could introduce error estimates based on model-to-model differences rather than relying solely on NR data. Additional nuisance parameters, such as higher-order PN terms or merger-ringdown fitted coefficients, may also be necessary for more extreme binary configurations. Our method addresses a specific source of error, related to the calibration of waveform models to NR, but does not account, e.g., for missing physical effects. Therefore, incorporating all relevant physical effects into waveform models remains essential. However, our results also indicate that this source of error would be significant in the near future, potentially as early as O5, and must be accounted for.

An advantage of our method is that, by using the native time-domain SEOBNRv5HM model, it can already be applied to its spin-precessing and eccentric BBH extensions, as well as systems containing NSs, to account for NR-calibration uncertainties in the quasi-circular aligned-spin BBH sector common to all the models. Once EOB models are calibrated to eccentric and spin-precessing NR simulations, our method can be extended to handle specific uncertainties related to these features. Our results with uniform priors on $\delta\theta$ also suggest that PE for spin-precessing and eccentric BBHs could be improved even without detailed calibration to NR, provided that reasonable priors can be set on appropriate calibration parameters. Our method could also enhance the robustness of tests of GR based on EOB waveforms [46, 136–139], and may help mitigate false GR deviation caused by waveform systematics [46, 138].

Acknowledgments – We are grateful to Arnab Dhani, Héctor Estellés, Jonathan Gair, Elise Sängner, Hector O. Silva and Alexandre Toubiana for valuable discussions. We also thank Cecilio Garcia-Quiros and Sebastian Khan for useful comments on the manuscript. The computational work for this manuscript was carried out on the Hypatia computer cluster at the Max Planck Institute for Gravitational Physics.

This study is similar to the recent work by Bachhar *et al.* [140], as both introduce a method for modeling waveform uncertainty from calibrating EOB models against NR data, and employ it in a Bayesian inference study. However, they differ significantly in how the uncertainty models are constructed and incorporated into PE.

-
- [1] B. P. Abbott *et al.* (LIGO Scientific, Virgo), *Phys. Rev. Lett.* **116**, 061102 (2016), arXiv:1602.03837 [gr-qc].
- [2] J. Aasi *et al.* (LIGO Scientific), *Class. Quant. Grav.* **32**, 074001 (2015), arXiv:1411.4547 [gr-qc].
- [3] F. Acernese *et al.* (VIRGO), *Class. Quant. Grav.* **32**, 024001 (2015), arXiv:1408.3978 [gr-qc].
- [4] T. Akutsu *et al.* (KAGRA), *PTEP* **2021**, 05A101 (2021), arXiv:2005.05574 [physics.ins-det].
- [5] R. Abbott *et al.* (KAGRA, VIRGO, LIGO Scientific), *Phys. Rev. X* **13**, 041039 (2023), arXiv:2111.03606 [gr-qc].
- [6] A. H. Nitz, S. Kumar, Y.-F. Wang, S. Kastha, S. Wu, M. Schäfer, R. Dhurkunde, and C. D. Capano, *Astrophys. J.* **946**, 59 (2023), arXiv:2112.06878 [astro-ph.HE].
- [7] A. K. Mehta, S. Olsen, D. Wadekar, J. Roulet, T. Venumadhav, J. Mushkin, B. Zackay, and M. Zaldarriaga, (2023), arXiv:2311.06061 [gr-qc].
- [8] R. Abbott *et al.* (KAGRA, VIRGO, LIGO Scientific), *Phys. Rev. X* **13**, 011048 (2023), arXiv:2111.03634 [astro-ph.HE].
- [9] B. P. Abbott *et al.* (LIGO Scientific, Virgo), *Phys. Rev. Lett.* **121**, 161101 (2018), arXiv:1805.11581 [gr-qc].
- [10] B. P. Abbott *et al.* (LIGO Scientific, Virgo, IM2H, Dark Energy Camera GW-E, DES, DLT40, Las Cumbres Observatory, VINROUGE, MASTER), *Nature* **551**, 85 (2017), arXiv:1710.05835 [astro-ph.CO].
- [11] R. Abbott *et al.* (LIGO Scientific, VIRGO, KAGRA), (2021), arXiv:2111.03604 [astro-ph.CO].
- [12] B. P. Abbott *et al.* (LIGO Scientific, Virgo), *Phys. Rev. Lett.* **116**, 221101 (2016), [Erratum: *Phys.Rev.Lett.* **121**, 129902 (2018)], arXiv:1602.03841 [gr-qc].
- [13] R. Abbott *et al.* (LIGO Scientific, VIRGO, KAGRA), (2021), arXiv:2112.06861 [gr-qc].
- [14] A. Buonanno, G. B. Cook, and F. Pretorius, *Phys. Rev. D* **75**, 124018 (2007), arXiv:gr-qc/0610122.
- [15] T. Damour and A. Nagar, *Phys. Rev. D* **77**, 024043 (2008), arXiv:0711.2628 [gr-qc].
- [16] P. Ajith *et al.*, *Class. Quant. Grav.* **24**, S689 (2007), arXiv:0704.3764 [gr-qc].
- [17] A. Taracchini, Y. Pan, A. Buonanno, E. Barausse, M. Boyle, T. Chu, G. Lovelace, H. P. Pfeiffer, and M. A. Scheel, *Phys. Rev. D* **86**, 024011 (2012), arXiv:1202.0790 [gr-qc].
- [18] S. Khan, S. Husa, M. Hannam, F. Ohme, M. Pürrer, X. Jiménez Forteza, and A. Bohé, *Phys. Rev. D* **93**, 044007 (2016), arXiv:1508.07253 [gr-qc].
- [19] A. Bohé *et al.*, *Phys. Rev. D* **95**, 044028 (2017), arXiv:1611.03703 [gr-qc].
- [20] J. Blackman, S. E. Field, M. A. Scheel, C. R. Galley, C. D. Ott, M. Boyle, L. E. Kidder, H. P. Pfeiffer, and B. Szilágyi, *Phys. Rev. D* **96**, 024058 (2017), arXiv:1705.07089 [gr-qc].
- [21] A. Nagar *et al.*, *Phys. Rev. D* **98**, 104052 (2018), arXiv:1806.01772 [gr-qc].
- [22] V. Varma, S. E. Field, M. A. Scheel, J. Blackman, D. Gerosa, L. C. Stein, L. E. Kidder, and H. P. Pfeiffer, *Phys. Rev. Research* **1**, 033015 (2019), arXiv:1905.09300 [gr-qc].
- [23] S. Ossokine *et al.*, *Phys. Rev. D* **102**, 044055 (2020), arXiv:2004.09442 [gr-qc].
- [24] G. Pratten *et al.*, *Phys. Rev. D* **103**, 104056 (2021), arXiv:2004.06503 [gr-qc].
- [25] H. Estellés, M. Colleoni, C. García-Quirós, S. Husa, D. Keitel, M. Mateu-Lucena, M. d. L. Planas, and A. Ramos-Buades, *Phys. Rev. D* **105**, 084040 (2022), arXiv:2105.05872 [gr-qc].
- [26] R. Gamba, S. Akçay, S. Bernuzzi, and J. Williams, *Phys. Rev. D* **106**, 024020 (2022), arXiv:2111.03675 [gr-qc].
- [27] A. Nagar, P. Retteno, R. Gamba, S. Albanesi, A. Albertini, and S. Bernuzzi, *Phys. Rev. D* **108**, 124018 (2023), arXiv:2304.09662 [gr-qc].
- [28] L. Pompili *et al.*, *Phys. Rev. D* **108**, 124035 (2023), arXiv:2303.18039 [gr-qc].
- [29] A. Ramos-Buades, A. Buonanno, H. Estellés, M. Khalil, D. P. Mihaylov, S. Ossokine, L. Pompili, and M. Shiferaw, *Phys. Rev. D* **108**, 124037 (2023), arXiv:2303.18046 [gr-qc].
- [30] J. E. Thompson, E. Hamilton, L. London, S. Ghosh, P. Kolitidou, C. Hoy, and M. Hannam, *Phys. Rev. D* **109**, 063012 (2024), arXiv:2312.10025 [gr-qc].
- [31] N. Afshordi *et al.* (LISA Consortium Waveform Working Group), (2023), arXiv:2311.01300 [gr-qc].
- [32] B. P. Abbott *et al.* (LIGO Scientific, Virgo), *Class. Quant. Grav.* **34**, 104002 (2017), arXiv:1611.07531 [gr-qc].
- [33] M. Pürrer and C.-J. Haster, *Phys. Rev. Res.* **2**, 023151 (2020), arXiv:1912.10055 [gr-qc].
- [34] Q. Hu and J. Veitch, *Phys. Rev. D* **106**, 044042 (2022), arXiv:2205.08448 [gr-qc].
- [35] T. Islam, A. Vajpeyi, F. H. Shaik, C.-J. Haster, V. Varma, S. E. Field, J. Lange, R. O’Shaughnessy, and R. Smith, (2023), arXiv:2309.14473 [gr-qc].
- [36] M. Punturo *et al.*, *Class. Quant. Grav.* **27**, 194002 (2010).
- [37] D. Reitze *et al.*, *Bull. Am. Astron. Soc.* **51**, 035 (2019), arXiv:1907.04833 [astro-ph.IM].
- [38] P. Amaro-Seoane *et al.* (LISA), (2017), arXiv:1702.00786 [astro-ph.IM].
- [39] S. Borhanian and B. S. Sathyaprakash, (2022), arXiv:2202.11048 [gr-qc].
- [40] R. Gamba, M. Breschi, S. Bernuzzi, M. Agathos, and A. Nagar, *Phys. Rev. D* **103**, 124015 (2021), arXiv:2009.08467 [gr-qc].
- [41] N. Kunert, P. T. H. Pang, I. Tews, M. W. Coughlin, and T. Dietrich, *Phys. Rev. D* **105**, L061301 (2022), arXiv:2110.11835 [astro-ph.HE].
- [42] C. B. Owen, C.-J. Haster, S. Perkins, N. J. Cornish, and N. Yunes, *Phys. Rev. D* **108**, 044018 (2023), arXiv:2301.11941 [gr-qc].
- [43] A. Dhani, S. Völkel, A. Buonanno, H. Estelles, J. Gair, H. P. Pfeiffer, L. Pompili, and A. Toubiana, (2024), arXiv:2404.05811 [gr-qc].
- [44] V. Kapil, L. Reali, R. Cotesta, and E. Berti, *Phys. Rev. D* **109**, 104043 (2024), arXiv:2404.00090 [gr-qc].
- [45] Q. Hu and J. Veitch, *Astrophys. J.* **945**, 103 (2023), arXiv:2210.04769 [gr-qc].
- [46] A. Toubiana, L. Pompili, A. Buonanno, J. R. Gair, and M. L. Katz, *Phys. Rev. D* **109**, 104019 (2024), arXiv:2307.15086

- [gr-qc].
- [47] A. Gupta *et al.*, (2024), arXiv:2405.02197 [gr-qc].
- [48] C. Foo and E. Hamilton, (2024), arXiv:2408.02671 [gr-qc].
- [49] F. Pretorius, *Phys. Rev. Lett.* **95**, 121101 (2005), arXiv:gr-qc/0507014.
- [50] M. Campanelli, C. O. Lousto, P. Marronetti, and Y. Zlochower, *Phys. Rev. Lett.* **96**, 111101 (2006), arXiv:gr-qc/0511048.
- [51] J. G. Baker, J. Centrella, D.-I. Choi, M. Koppitz, and J. van Meter, *Phys. Rev. Lett.* **96**, 111102 (2006), arXiv:gr-qc/0511103.
- [52] D. Ferguson, K. Jani, P. Laguna, and D. Shoemaker, *Phys. Rev. D* **104**, 044037 (2021), arXiv:2006.04272 [gr-qc].
- [53] A. Jan, D. Ferguson, J. Lange, D. Shoemaker, and A. Zimmerman, (2023), arXiv:2312.10241 [gr-qc].
- [54] A. Buonanno and T. Damour, *Phys. Rev. D* **59**, 084006 (1999), arXiv:gr-qc/9811091.
- [55] A. Buonanno and T. Damour, *Phys. Rev. D* **62**, 064015 (2000), arXiv:gr-qc/0001013.
- [56] T. Damour, P. Jaranowski, and G. Schaefer, *Phys. Rev. D* **62**, 084011 (2000), arXiv:gr-qc/0005034.
- [57] T. Damour, *Phys. Rev. D* **64**, 124013 (2001), arXiv:gr-qc/0103018.
- [58] A. Buonanno, Y. Chen, and T. Damour, *Phys. Rev. D* **74**, 104005 (2006), arXiv:gr-qc/0508067.
- [59] T. Futamase and Y. Itoh, *Living Rev. Rel.* **10**, 2 (2007).
- [60] L. Blanchet, *Living Rev. Rel.* **17**, 2 (2014), arXiv:1310.1528 [gr-qc].
- [61] A. Buonanno, Y. Pan, J. G. Baker, J. Centrella, B. J. Kelly, S. T. McWilliams, and J. R. van Meter, *Phys. Rev. D* **76**, 104049 (2007), arXiv:0706.3732 [gr-qc].
- [62] A. Nagar and P. Retegno, *Phys. Rev. D* **104**, 104004 (2021), arXiv:2108.02043 [gr-qc].
- [63] M. Khalil, A. Buonanno, H. Estelles, D. P. Mihaylov, S. Ossokine, L. Pompili, and A. Ramos-Buades, *Phys. Rev. D* **108**, 124036 (2023), arXiv:2303.18143 [gr-qc].
- [64] A. Nagar, R. Gamba, P. Retegno, V. Fantini, and S. Bernuzzi, (2024), arXiv:2404.05288 [gr-qc].
- [65] T. Damour, *Phys. Rev. D* **81**, 024017 (2010), arXiv:0910.5533 [gr-qc].
- [66] S. Akcay, L. Barack, T. Damour, and N. Sago, *Phys. Rev. D* **86**, 104041 (2012), arXiv:1209.0964 [gr-qc].
- [67] A. Le Tiec, E. Barausse, and A. Buonanno, *Phys. Rev. Lett.* **108**, 131103 (2012), arXiv:1111.5609 [gr-qc].
- [68] A. Antonelli, M. van de Meent, A. Buonanno, J. Steinhoff, and J. Vines, *Phys. Rev. D* **101**, 024024 (2020), arXiv:1907.11597 [gr-qc].
- [69] M. van de Meent, A. Buonanno, D. P. Mihaylov, S. Ossokine, L. Pompili, N. Warburton, A. Pound, B. Wardell, L. Durkan, and J. Miller, *Phys. Rev. D* **108**, 124038 (2023), arXiv:2303.18026 [gr-qc].
- [70] T. Damour, *Phys. Rev. D* **94**, 104015 (2016), arXiv:1609.00354 [gr-qc].
- [71] A. Antonelli, A. Buonanno, J. Steinhoff, M. van de Meent, and J. Vines, *Phys. Rev. D* **99**, 104004 (2019), arXiv:1901.07102 [gr-qc].
- [72] M. Khalil, A. Buonanno, J. Steinhoff, and J. Vines, *Phys. Rev. D* **106**, 024042 (2022), arXiv:2204.05047 [gr-qc].
- [73] T. Damour and P. Retegno, (2022), arXiv:2211.01399 [gr-qc].
- [74] P. Retegno, G. Pratten, L. M. Thomas, P. Schmidt, and T. Damour, *Phys. Rev. D* **108**, 124016 (2023), arXiv:2307.06999 [gr-qc].
- [75] A. Buonanno, G. U. Jakobsen, and G. Mogull, (2024), arXiv:2402.12342 [gr-qc].
- [76] A. Buonanno, G. Mogull, R. Patil, and L. Pompili, (2024), arXiv:2405.19181 [gr-qc].
- [77] Y. Pan, A. Buonanno, A. Taracchini, M. Boyle, L. E. Kidder, A. H. Mroué, H. P. Pfeiffer, M. A. Scheel, B. Szilágyi, and A. Zenginoglu, *Phys. Rev. D* **89**, 061501 (2014), arXiv:1311.2565 [gr-qc].
- [78] G. Ashton and S. Khan, *Phys. Rev. D* **101**, 064037 (2020), arXiv:1910.09138 [gr-qc].
- [79] A. Z. Jan, A. B. Yelikar, J. Lange, and R. O’Shaughnessy, *Phys. Rev. D* **102**, 124069 (2020), arXiv:2011.03571 [gr-qc].
- [80] G. Ashton and T. Dietrich, *Nature Astron.* **6**, 961 (2022), arXiv:2111.09214 [gr-qc].
- [81] C. Hoy, *Phys. Rev. D* **106**, 083003 (2022), arXiv:2208.00106 [gr-qc].
- [82] A. Puecher, A. Samajdar, G. Ashton, C. Van Den Broeck, and T. Dietrich, *Phys. Rev. D* **109**, 023019 (2024), arXiv:2310.03555 [gr-qc].
- [83] C. Hoy, S. Akcay, J. Mac Uilliam, and J. E. Thompson, (2024), arXiv:2409.19404 [gr-qc].
- [84] C. J. Moore and J. R. Gair, *Phys. Rev. Lett.* **113**, 251101 (2014), arXiv:1412.3657 [gr-qc].
- [85] J. R. Gair and C. J. Moore, *Phys. Rev. D* **91**, 124062 (2015), arXiv:1504.02767 [gr-qc].
- [86] C. J. Moore, C. P. L. Berry, A. J. K. Chua, and J. R. Gair, *Phys. Rev. D* **93**, 064001 (2016), arXiv:1509.04066 [gr-qc].
- [87] Z. Doctor, B. Farr, D. E. Holz, and M. Pürrer, *Phys. Rev. D* **96**, 123011 (2017), arXiv:1706.05408 [astro-ph.HE].
- [88] D. Williams, I. S. Heng, J. Gair, J. A. Clark, and B. Khamessa, *Phys. Rev. D* **101**, 063011 (2020), arXiv:1903.09204 [gr-qc].
- [89] T. Andrade, R. Gamba, and J. Trenado, (2023), arXiv:2311.11311 [gr-qc].
- [90] S. Khan, *Phys. Rev. D* **109**, 104045 (2024), arXiv:2403.11534 [gr-qc].
- [91] B. Edelman *et al.*, *Phys. Rev. D* **103**, 042004 (2021), arXiv:2008.06436 [gr-qc].
- [92] J. S. Read, *Class. Quant. Grav.* **40**, 135002 (2023), arXiv:2301.06630 [gr-qc].
- [93] M. Breschi, S. Bernuzzi, D. Godzieba, A. Perego, and D. Radice, *Phys. Rev. Lett.* **128**, 161102 (2022), arXiv:2110.06957 [gr-qc].
- [94] M. Breschi, S. Bernuzzi, K. Chakravarti, A. Camilletti, A. Prakash, and A. Perego, *Phys. Rev. D* **109**, 064009 (2024), arXiv:2205.09112 [gr-qc].
- [95] M. Breschi, R. Gamba, G. Carullo, D. Godzieba, S. Bernuzzi, A. Perego, and D. Radice, *Astron. Astrophys.* **689**, A51 (2024), arXiv:2401.03750 [astro-ph.HE].
- [96] D. P. Mihaylov, S. Ossokine, A. Buonanno, H. Estelles, L. Pompili, M. Pürrer, and A. Ramos-Buades, (2023), arXiv:2303.18203 [gr-qc].
- [97] V. Varma, S. E. Field, M. A. Scheel, J. Blackman, L. E. Kidder, and H. P. Pfeiffer, *Phys. Rev. D* **99**, 064045 (2019), arXiv:1812.07865 [gr-qc].
- [98] M. Boyle *et al.*, *Class. Quant. Grav.* **36**, 195006 (2019), arXiv:1904.04831 [gr-qc].
- [99] A. H. Mroué *et al.*, *Phys. Rev. Lett.* **111**, 241104 (2013), arXiv:1304.6077 [gr-qc].
- [100] D. A. Hemberger, G. Lovelace, T. J. Loredo, L. E. Kidder, M. A. Scheel, B. Szilágyi, N. W. Taylor, and S. A. Teukolsky, *Phys. Rev. D* **88**, 064014 (2013), arXiv:1305.5991 [gr-qc].
- [101] M. A. Scheel, M. Giesler, D. A. Hemberger, G. Lovelace, K. Kuper, M. Boyle, B. Szilágyi, and L. E. Kidder, *Class. Quant. Grav.* **32**, 105009 (2015), arXiv:1412.1803 [gr-qc].
- [102] G. Lovelace *et al.*, *Class. Quant. Grav.* **32**, 065007 (2015),

- arXiv:1411.7297 [gr-qc].
- [103] T. Chu, H. Fong, P. Kumar, H. P. Pfeiffer, M. Boyle, D. A. Hemberger, L. E. Kidder, M. A. Scheel, and B. Szilágyi, *Class. Quant. Grav.* **33**, 165001 (2016), arXiv:1512.06800 [gr-qc].
- [104] J. Blackman, S. E. Field, C. R. Galley, B. Szilágyi, M. A. Scheel, M. Tiglio, and D. A. Hemberger, *Phys. Rev. Lett.* **115**, 121102 (2015), arXiv:1502.07758 [gr-qc].
- [105] B. P. Abbott *et al.* (LIGO Scientific, Virgo), *Phys. Rev. Lett.* **116**, 241103 (2016), arXiv:1606.04855 [gr-qc].
- [106] B. P. Abbott *et al.* (LIGO Scientific, Virgo), *Phys. Rev. D* **94**, 064035 (2016), arXiv:1606.01262 [gr-qc].
- [107] G. Lovelace *et al.*, *Class. Quant. Grav.* **33**, 244002 (2016), arXiv:1607.05377 [gr-qc].
- [108] J. Blackman, S. E. Field, M. A. Scheel, C. R. Galley, D. A. Hemberger, P. Schmidt, and R. Smith, *Phys. Rev. D* **95**, 104023 (2017), arXiv:1701.00550 [gr-qc].
- [109] J. Yoo, V. Varma, M. Giesler, M. A. Scheel, C.-J. Haster, H. P. Pfeiffer, L. E. Kidder, and M. Boyle, *Phys. Rev. D* **106**, 044001 (2022), arXiv:2203.10109 [gr-qc].
- [110] S. R. Brandt *et al.*, “The einstein toolkit,” (2024).
- [111] C. M. Bishop, “Mixture density networks,” (1994).
- [112] T. Damour, B. R. Iyer, and A. Nagar, *Phys. Rev. D* **79**, 064004 (2009), arXiv:0811.2069 [gr-qc].
- [113] T. Damour and A. Nagar, *Phys. Rev. D* **76**, 064028 (2007), arXiv:0705.2519 [gr-qc].
- [114] Y. Pan, A. Buonanno, R. Fujita, E. Racine, and H. Tagoshi, *Phys. Rev. D* **83**, 064003 (2011), [Erratum: *Phys. Rev. D* **87**, 109901 (2013)], arXiv:1006.0431 [gr-qc].
- [115] Y. Pan, A. Buonanno, M. Boyle, L. T. Buchman, L. E. Kidder, H. P. Pfeiffer, and M. A. Scheel, *Phys. Rev. D* **84**, 124052 (2011), arXiv:1106.1021 [gr-qc].
- [116] J. G. Baker, W. D. Boggs, J. Centrella, B. J. Kelly, S. T. McWilliams, and J. R. van Meter, *Phys. Rev. D* **78**, 044046 (2008), arXiv:0805.1428 [gr-qc].
- [117] T. Damour and A. Nagar, *Phys. Rev. D* **90**, 024054 (2014), arXiv:1406.0401 [gr-qc].
- [118] R. Cotesta, A. Buonanno, A. Bohé, A. Taracchini, I. Hinder, and S. Ossokine, *Phys. Rev. D* **98**, 084028 (2018), arXiv:1803.10701 [gr-qc].
- [119] J. M. Bardeen, W. H. Press, and S. A. Teukolsky, *Astrophys. J.* **178**, 347 (1972).
- [120] X. Jiménez-Forteza, D. Keitel, S. Husa, M. Hannam, S. Khan, and M. Pürrer, *Phys. Rev. D* **95**, 064024 (2017), arXiv:1611.00332 [gr-qc].
- [121] F. Hofmann, E. Barausse, and L. Rezzolla, *Astrophys. J. Lett.* **825**, L19 (2016), arXiv:1605.01938 [gr-qc].
- [122] B. S. Sathyaprakash and S. V. Dhurandhar, *Phys. Rev. D* **44**, 3819 (1991).
- [123] L. S. Finn and D. F. Chernoff, *Phys. Rev. D* **47**, 2198 (1993), arXiv:gr-qc/9301003.
- [124] G. Ashton *et al.*, *Astrophys. J. Suppl.* **241**, 27 (2019), arXiv:1811.02042 [astro-ph.IM].
- [125] J. Skilling, *Bayesian Analysis* **1**, 833 (2006).
- [126] M. J. Williams, J. Veitch, and C. Messenger, *Phys. Rev. D* **103**, 103006 (2021), arXiv:2102.11056 [gr-qc].
- [127] A. Paszke *et al.*, (2019), arXiv:1912.01703 [cs.LG].
- [128] P. Schmidt, I. W. Harry, and H. P. Pfeiffer, (2017), arXiv:1703.01076 [gr-qc].
- [129] R. J. E. Smith, G. Ashton, A. Vajpeyi, and C. Talbot, *Mon. Not. Roy. Astron. Soc.* **498**, 4492 (2020), arXiv:1909.11873 [gr-qc].
- [130] I. M. Romero-Shaw *et al.*, *Mon. Not. Roy. Astron. Soc.* **499**, 3295 (2020), arXiv:2006.00714 [astro-ph.IM].
- [131] J. S. Speagle, *Mon. Not. Roy. Astron. Soc.* **493**, 3132 (2020), arXiv:1904.02180 [astro-ph.IM].
- [132] “Noise curves used for simulations in the update of the observing scenarios paper,” (2022), LIGO Document T2000012-v2.
- [133] B. P. Abbott *et al.* (KAGRA, LIGO Scientific, Virgo, VIRGO), *Living Rev. Rel.* **21**, 3 (2018), arXiv:1304.0670 [gr-qc].
- [134] “A# strain sensitivity,” (2022), LIGO Document T2300041-v1.
- [135] It would be more realistic to consider the ET starting from a lower frequency of 3 – 5 Hz. However, the accuracy of current long NR waveforms is likely insufficient for this, as their accuracy during the inspiral phase is compromised by accumulated phase errors. This also makes it difficult to quantify the accuracy of hybridized NR surrogate waveforms, which we use to simulate signals, for such long signals [97].
- [136] R. Brito, A. Buonanno, and V. Raymond, *Phys. Rev. D* **98**, 084038 (2018), arXiv:1805.00293 [gr-qc].
- [137] A. Ghosh, R. Brito, and A. Buonanno, *Phys. Rev. D* **103**, 124041 (2021), arXiv:2104.01906 [gr-qc].
- [138] E. Maggio, H. O. Silva, A. Buonanno, and A. Ghosh, (2022), arXiv:2212.09655 [gr-qc].
- [139] A. K. Mehta, A. Buonanno, R. Cotesta, A. Ghosh, N. Sennett, and J. Steinhoff, *Phys. Rev. D* **107**, 044020 (2023), arXiv:2203.13937 [gr-qc].
- [140] R. Bachhar, M. Pürrer, and S. R. Green, “Incorporating waveform calibration error in gravitational-wave modeling and inference for SEOBNRv4,” In prep.
- [141] M. Branchesi *et al.*, *JCAP* **07**, 068 (2023), arXiv:2303.15923 [gr-qc].
- [142] H. Estellés Estrella, S. Ossokine, and D. Williams, “pe-configurator,” (2023).
- [143] J. Kruse, *CoRR abs/2003.05739* (2020), 2003.05739.
- [144] F. Pedregosa, G. Varoquaux, A. Gramfort, V. Michel, B. Thirion, O. Grisel, M. Blondel, P. Prettenhofer, R. Weiss, V. Dubourg, J. Vanderplas, A. Passos, D. Cournapeau, M. Brucher, M. Perrot, and E. Duchesnay, *Journal of Machine Learning Research* **12**, 2825 (2011).
- [145] L. Barsotti, P. Fritschel, M. Evans, and S. Gras (LIGO Collaboration), “Updated advanced ligo sensitivity design curve,” (2018), LIGO Document T1800044-v5.

SUPPLEMENTAL MATERIAL

Detector networks

Current GW detectors are projected to reach their design sensitivity within the next few years during the fifth observing run (O5) and will continue to operate until the end of the decade [133]. Following this period, significant upgrades are anticipated, with the expectation that detectors might remain operational until the advent of XG detectors. In this work, we consider four GW ground-based detector networks, consisting of current detectors at their design and upgraded sensitivities, and a configuration where upgraded current detectors work in conjunction with an XG detector. These are listed below:

- **O4 network:** This network comprises the advanced LIGO detectors at Hanford and Livingston operating at O4 sensitivity, and the advanced Virgo detector operating at design sensitivity. We use the noise curves available in Bilby, specifically aLIGO O4 high [132] and Adv [133]. The minimum frequency is set to $f_{\text{low}} = 20$ Hz.
- **O5 network:** This network includes the advanced LIGO detectors at Hanford and Livingston operating at design (A+) sensitivity, using the same noise curve as in [43], along with the advanced Virgo detector at design sensitivity. The minimum frequency is set to $f_{\text{low}} = 15$ Hz.
- **A# network:** This network consists of the advanced LIGO detectors at Hanford and Livingston operating at A# sensitivity, using the same noise curve as in [43], and the advanced Virgo detector at design sensitivity. The minimum frequency is set to $f_{\text{low}} = 10$ Hz.
- **ET-A# network:** This network includes a 10 km ET in Europe, at the Virgo location, using the same noise curve as in [43], combined with LIGO detectors at Hanford and Livingston operating at A# sensitivity. Although the ET is proposed to have a triangular configuration, the `bilby` pipe wrapper is limited to L-shaped interferometer configurations. Therefore, we assume the ET to be L-shaped as in Ref. [43]. This does not significantly impact our results as the shape of the interferometer is not critical to the conclusions discussed here [141]. The minimum frequency at which we start integrating the likelihood is set to $f_{\text{low}} = 10$ Hz. While it would be more realistic to consider the ET starting from a lower frequency of $\sim 3 - 5$ Hz, the accuracy of long NR simulations and of hybridized NR surrogate waveforms, which we use to simulate signals, is not guaranteed to be sufficient for such long signals [97].

The amplitude-spectral-density (ASD) curves of the individual detectors are shown in Fig. 4. The details of the detector networks are further summarized in Table I, together with the segment length and the network optimal SNR, for the binary configurations considered in this study. The maximum frequency is $f_{\text{high}} = 1024$ Hz for all networks, which is above the rolloff frequency of the higher-order modes for all the sys-

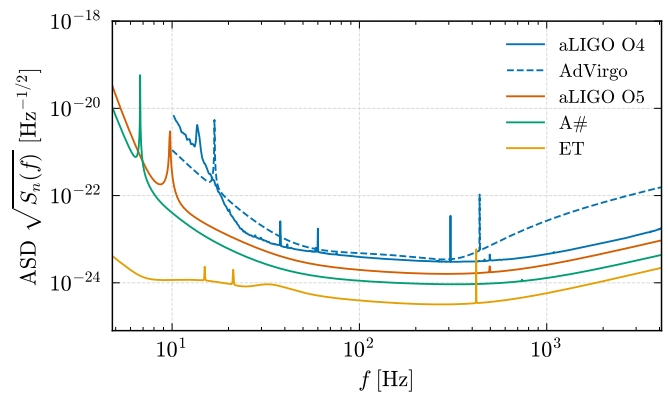


Figure 4. The amplitude-spectral-density curves of the various detectors used in this paper. The curves labeled by aLIGO O4 and AdVirgo denote the sensitivity of the LIGO detectors during the fourth observing run, and the design sensitivity of the Virgo detector, respectively. The aLIGO O5 and A# curves refer to the design (A+) and upgraded sensitivity of the LIGO detectors, respectively.

tems considered in this work. The sampling frequency is then chosen to be $f_s = 2048$ Hz. We determined optimal analysis settings with the `PE configurator` package [142].

Proposed XG detector networks often include the ET operating in conjunction with one or more CE detectors. The sources we consider would have an SNR around 1500 in such a network. For such high SNRs, the accuracy of current NR waveforms may not be adequate [33], potentially complicating efforts to identify the origins of any biases. As a result, we do not explore these configurations.

Details of the MDN model and sanity checks

This section provides technical details about the neural network architecture and summarizes some of the sanity checks that we performed to assess the robustness of our model.

We implement the MDN model using the PyTorch framework [127]. Specifically, we construct the network using a Sequential container comprising multiple Linear layers. To introduce non-linearity within the network layers, we apply a Leaky ReLU (LReLU) activation function. The training process involves minimizing the following loss function with respect to the network weights w ,

$$L(w) = -\frac{1}{N} \sum_{n=1}^N \ln \left[\sum_{k=1}^K \pi_k \left(\mathbf{\Lambda}^{(n)}, w \right) \times \mathcal{N} \left(\theta^{(n)} \mid \mu_k \left(\mathbf{\Lambda}^{(n)}, w \right), \Sigma_k \left(\mathbf{\Lambda}^{(n)}, w \right) \right) \right]. \quad (3)$$

Here, $\mathcal{N}(\theta \mid \mu, \Sigma)$ are multivariate Gaussian distributions with mean μ and covariance matrix Σ , e.g., $\mathcal{N}(\theta \mid \mu, \Sigma) \propto \exp \left[-\frac{1}{2} (\theta - \mu)^T \Sigma^{-1} (\theta - \mu) \right]$, π_k are the weights of the K Gaussians in the mixture, and N is the number of NR-calibration posteriors used for training. This loss function represents the mean of the negative log-posterior of the

| Network | List of Interferometers and PSD | f_{low} [Hz] | Segment length [s] | Network SNR | |
|---------|----------------------------------|-----------------------|--------------------|--------------|--------------|
| | | | | $\chi_i > 0$ | $\chi_i < 0$ |
| O4 | H1, L1 (aLIGO O4 high), V1 (AdV) | 20 | 8 | 51.75 | 39.27 |
| O5 | H1, L1 (A+), V1 (AdV) | 15 | 8 | 91.67 | 69.95 |
| A# | H1, L1 (A#), V1 (AdV) | 10 | 16 | 163.28 | 125.64 |
| ET-A# | H1, L1 (A#), ET (ET-D) | 10 | 16 | 439.23 | 366.72 |

Table I. Detector networks used in this study. The networks are defined by the list of interferometers, with their PSD in parentheses. We also indicate the frequency f_{low} at which we start integrating the likelihood integral and the network SNR of the NRHybSur3dq8 signals in these networks (see the main text for the parameters).

MDN [143]. We use full covariance matrices, which we parametrize by their Cholesky decomposition.

We use the Adam optimization algorithm for training the network. We initially determine a set of model hyper-parameters (number of Gaussians in the mixture, number of network layers, `n_layers`, number of neurons per layer, `n_neurons`, and number of training epochs, `n_epochs`) with an 80-20 training-test split. These hyper-parameters are further refined by performing waveform sanity checks against NRHybSur3dq8 waveforms not included in the training set. Our final settings are `n_layers` = 6, `n_neurons` = 96, `n_epochs` = 5000 and a single Gaussian component.

We transform the variables Λ from (q, χ_1, χ_2) to $(\nu, \chi_{\text{eff}}, \chi_a)$. As mentioned in the main text, to improve the extrapolation behavior of the model, we fit the residuals of the calibration parameters θ after subtracting the least-square fits of Ref. [28] (with the superscript $\nu 5$), which we denote $(\delta\Delta t_{\text{NR}}, \delta d_{\text{SO}}) \equiv \delta\theta$. Test-particle ($\nu \rightarrow 0$) information is already enforced by the least-square fits, so we rescale the residual posteriors by ν to have the correction go to zero in that limit. In the small-spin limit, the posteriors are uninformative because the model is already well-calibrated, and the term containing d_{SO} in H_{EOB} is scaled by a χ_{eff} factor [63]. To recover the non-spinning limit of the model, and improve its robustness for small-spin configurations, we taper the corrections with a tanh function

$$\begin{aligned} \Delta t_{\text{NR}} &= \Delta t_{\text{NR}}^{\nu 5}(\nu, \chi_{\text{eff}}, \chi_a) + \nu \tanh\left[\alpha\left(\chi_{\text{eff}}^2 + \chi_a^2\right)\right] \Delta t_{\text{NR}}^{\text{MDN}}(\nu, \chi_{\text{eff}}, \chi_a) \\ &\equiv \Delta t_{\text{NR}}^{\nu 5}(\nu, \chi_{\text{eff}}, \chi_a) + \delta\Delta t_{\text{NR}}, \end{aligned} \quad (4a)$$

$$\begin{aligned} d_{\text{SO}} &= d_{\text{SO}}^{\nu 5}(\nu, \chi_{\text{eff}}, \chi_a) + \nu \tanh\left[\alpha\left(\chi_{\text{eff}}^2 + \chi_a^2\right)\right] d_{\text{SO}}^{\text{MDN}}(\nu, \chi_{\text{eff}}, \chi_a) \\ &\equiv d_{\text{SO}}^{\nu 5}(\nu, \chi_{\text{eff}}, \chi_a) + \delta d_{\text{SO}}. \end{aligned} \quad (4b)$$

We choose $\alpha = 10$ based on sanity checks against NR and NRHybSur3dq8 waveforms not used in the training. Before performing the fit, we finally apply a `StandardScaler` transformation with `scikit-learn` [144], such that the data have a mean of zero and a standard deviation of one.

To quantify the similarity between the NR-calibration posteriors residuals, $p(\delta\theta | \Lambda)$, and our MDN fit, we show in Fig. 5 the Jensen-Shannon divergence (JSD) between 1D marginalized distributions of $\delta\theta = (\delta\Delta t_{\text{NR}}, \delta d_{\text{SO}})$, for the 400 spinning NR simulations employed to build the model. The JSD ranges between 0 and 1 bits, with the similarity between the distributions being greater when the JSD is closer to zero. The JSD between two distributions $p(\vartheta)$ and $q(\vartheta)$ is defined

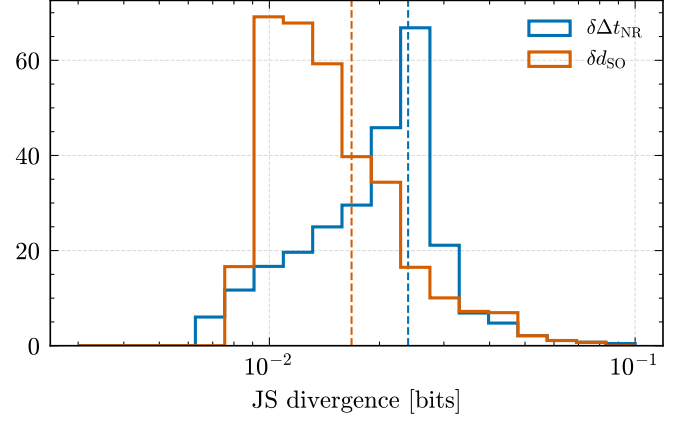


Figure 5. JSD between the 1D marginalized distributions of $(\delta\Delta t_{\text{NR}}, \delta d_{\text{SO}})$ for NR-calibration posteriors residuals, $p(\delta\theta | \Lambda)$, and our MDN fit, across the 400 spinning NR simulations used to build the model. The vertical dashed lines indicate the median of the distributions.

as a symmetrized version of the Kullback-Leibler (KL) divergence:

$$\text{JSD} = \frac{D_{\text{KL}}(p|q) + D_{\text{KL}}(q|p)}{2}, \quad (5)$$

where the KL divergence is defined as

$$D_{\text{KL}}(p|q) = \int d\vartheta p(\vartheta) \log_2 \left(\frac{p(\vartheta)}{q(\vartheta)} \right). \quad (6)$$

For both $(\delta\Delta t_{\text{NR}}, \delta d_{\text{SO}})$ the median JSD, indicated by the vertical dashed lines, is around 0.02 bits.

As an illustrative example, we compare in Fig. 6 the NR-calibration posterior residual $p(\delta\theta | \Lambda)$ and the corresponding MDN fit, for the NR simulation `SXS:BBH:2158` with parameters $\Lambda = (q, \chi_1, \chi_2) \approx (3.0, 0.5, 0.5)$. This is a representative case with $\text{JSD} \approx 0.022$ for $\delta\Delta t_{\text{NR}}$ and $\text{JSD} \approx 0.017$ for δd_{SO} . Note that the posterior encompasses zero, indicated by the black lines, which corresponds to the default `SEOBNRv5HM` fit. The largest JSD values correspond to broader, more uninformative posteriors, which are harder to fit accurately. These occur particularly near non-spinning or negative-spin configurations. However, this is not a significant issue since uninformative posteriors indicate that the default `SEOBNRv5HM` model is already accurate.

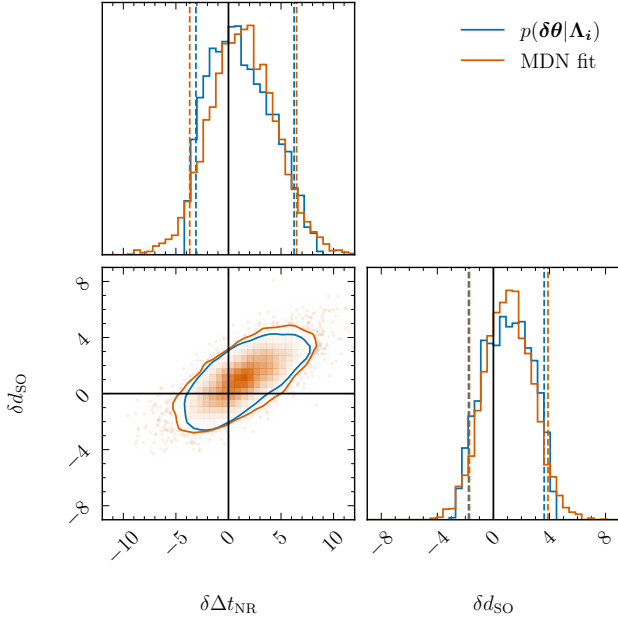


Figure 6. Comparison of the NR-calibration posterior residual $p(\delta\theta | \Lambda_i)$ and the corresponding MDN fit, for the NR simulation SXS:BBH:2158 with parameters $\Lambda_i = (q, \chi_1, \chi_2) \simeq (3.0, 0.5, 0.5)$. This case has $\text{JSD} \simeq 0.022$ for $\delta\Delta t_{\text{NR}}$ and $\text{JSD} \simeq 0.017$ for δd_{SO} . Note that the posterior encompasses zero, indicated by the black lines, which corresponds to the default SEOBNRv5HM fit.

We now turn to waveform sanity checks, computing the maximum (2,2)-mode mismatch over a range of total masses between 10 and 300 M_\odot using the aLIGO PSD [145] for different SEOBNRv5 variations. We compare the default SEOBNRv5 model, a version of SEOBNRv5 using the mean of the MDN fit of $p(\delta\theta | \Lambda)$ for $\delta\theta$, and one in which we take median mismatch over 100 samples for $\delta\theta$ from the MDN model.

In the top panel of Fig. 7, we compare the three SEOBNRv5 variations against the 442 NR simulations used in this work, showing the cumulative distribution of the maximum mismatch. We also include 42 non-spinning simulations, not used to build the MDN model, to allow a direct comparison with the results of Ref. [28]. We observe that using the mean of the MDN fit for $\delta\theta$ results in a more NR-faithful model than the default SEOBNRv5. The median of the distribution, indicated by the vertical dashed lines, decreases by almost a factor of 2 from 2.1×10^{-4} to 1.1×10^{-4} . Additionally, the fraction of cases with maximum mismatch $\lesssim 1 \times 10^{-3}$ increases from 90% to 96%. Using different samples for $\delta\theta$ from the MDN fit also provides comparable accuracy, mostly below the $\sim 1 \times 10^{-3}$ level, consistent with the likelihood function used in the calibration (2). The median mismatch is 3.6×10^{-4} , with about 92% of cases having a mismatch $\lesssim 1 \times 10^{-3}$.

In the bottom panel of Fig. 7, we compare the three SEOBNRv5 variations to NRHybSur3dq8 waveforms, which were not used in the training process. We use 5000 random configurations with $q \in [1, 8]$, $|\chi_i| \leq 0.9$ and a dimensionless orbital frequency $M\Omega_0 = 0.015$, allowing some extrap-

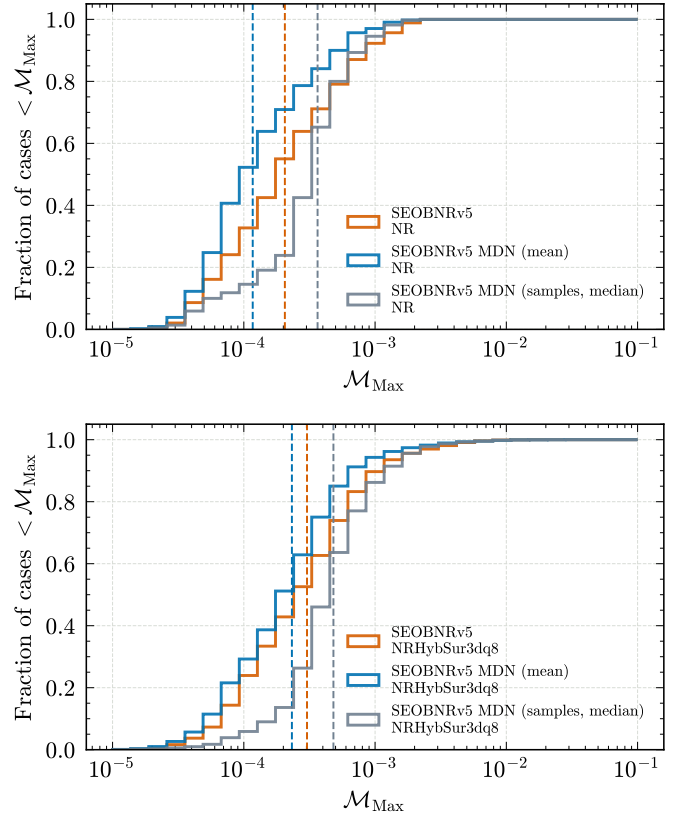


Figure 7. *Top panel:* cumulative distribution of the maximum (2,2)-mode mismatch over 10 and 300 M_\odot , against the 442 NR simulations used in this work. *Bottom panel:* cumulative distribution of the maximum (2,2)-mode mismatch over 10 and 300 M_\odot , against NRHybSur3dq8, for 5000 random configurations with $q \in [1, 8]$, $|\chi_i| \leq 0.9$. The vertical dashed lines show the medians. In both panels, we compare the results of the default SEOBNRv5 model, a version of SEOBNRv5 using the mean of the MDN fit of $p(\delta\theta | \Lambda)$ for $\delta\theta$, and one in which we take median mismatch over 100 samples for $\delta\theta$ from the MDN model.

olation outside the surrogate’s training region ($|\chi_i| \leq 0.8$) to test the extrapolation of the MDN fit. The mismatch values are comparable to the ones against NR, albeit slightly higher because of the larger number of challenging cases with high q and high spin in this comparison. The SEOBNRv5 version using the mean of the MDN fit for $\delta\theta$ outperforms the default SEOBNRv5 model, with the median mismatch decreasing from 3.0×10^{-4} to 2.3×10^{-4} and fraction of cases with mismatch $\lesssim 1 \times 10^{-3}$ increasing from 87% to 93%. This confirms that, regardless of the uncertainty estimate, the MDN fit is a more flexible method compared to the hierarchical least-square fits used in the default SEOBNRv5 model. It captures subdominant features present in the NR data without overfitting. Also in this case, taking different samples for $\delta\theta$ from the MDN also provides comparable performance and confirms that the uncertainty estimate leads to well-behaved waveforms overall. The median mismatch in this case is 4.8×10^{-4} , with about 83% of cases having a mismatch $\lesssim 1 \times 10^{-3}$.

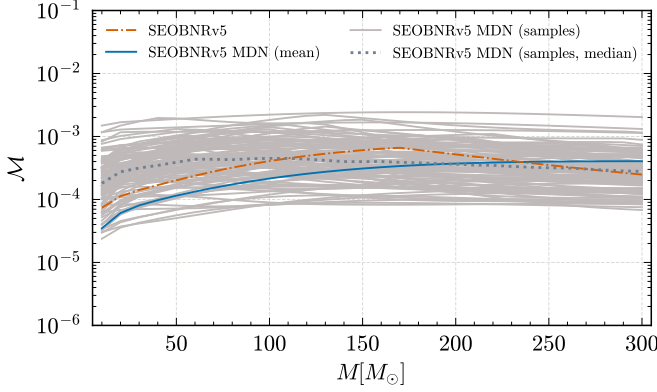


Figure 8. Mismatch distribution as a function of the total mass between NRHybSur3dq8 and different variations of SEOBNRv5, for $\Lambda = (q, \chi_1, \chi_2) = (3.0, 0.45, 0.45)$. We show the default SEOBNRv5 model and variations which use the mean or different samples of the MDN fit for $\delta\theta$.

Finally, Fig. 8 shows an example of the mismatch distribution as a function of the total mass for 100 samples from the MDN model. The mismatch is computed against NRHybSur3dq8, with parameters $\Lambda = (q, \chi_1, \chi_2) = (3.0, 0.45, 0.45)$, as the case shown in Fig. 1. The darker dotted line indicates the median mismatch across the 100 samples, while the default SEOBNRv5 model and the version using the mean of the MDN fit for $\delta\theta$ are represented by the orange and blue lines, respectively.

Impact of higher-modes mismodeling

In this appendix, we present PE results for the positive-spin configuration, with $q = 3$ and $\chi_i = 0.45$, for upcoming runs, O4, O5, A#, and next-generation ground-based detector networks (ET-A#). As for the other runs, PE is performed by injecting a NRHybSur3dq8 signal and recovering it using SEOBNRv5HM, either sampling only the standard source parameters, or including corrections to the NR-calibration parameters $\delta\theta$, with either uniform or $p(\delta\theta | \Lambda)$ priors, reflecting NR-calibration uncertainty.

Figure 9 is the equivalent of Fig. 3, but for the positive-spin configuration. It shows the ratio of systematic bias to statistical errors ($\delta\lambda/\Delta\lambda$) as a function of the network SNR in the top panel, and the ratio of statistical errors ($\Delta\lambda$) with and without corrections to the NR-calibration parameters $\delta\theta$, in the bottom panel. For the O5 and A# detector networks, where the injected signal has SNR ~ 100 , accounting for NR-calibration uncertainties by sampling over the $\delta\theta$ parameters substantially mitigates the biases recovered by the SEOBNRv5HM model. This is not true in the ET-A# network, in which the injected signal has SNR = 439.23, although biases are still slightly reduced, especially when looking at 2D marginalized posterior distributions. The presence of a bias suggests that the $\delta\theta$ parameters do not provide suffi-

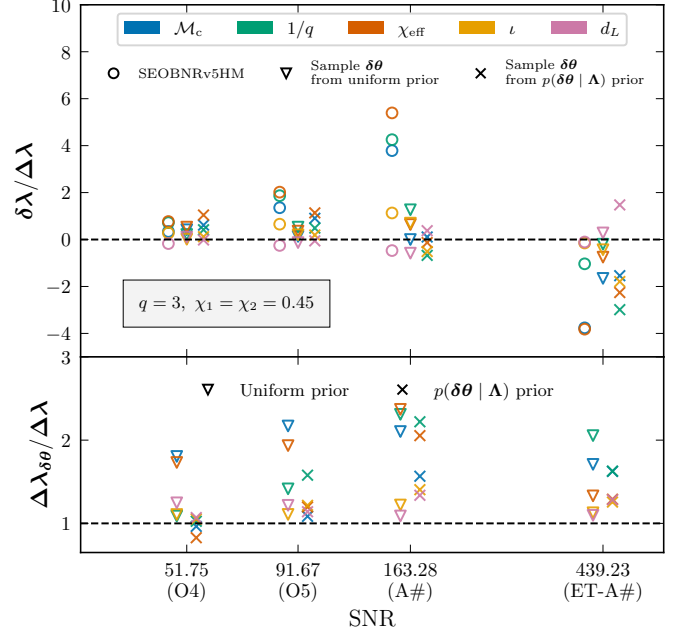


Figure 9. Same as the left panel of Fig. 3, but for the positive-spin configuration, with $q = 3$ and $\chi_i = 0.45$. *Top*: Ratio of systematic bias to statistical errors ($\delta\lambda/\Delta\lambda$) as a function of the network SNR. *Bottom*: Ratio of statistical errors ($\Delta\lambda$) with and without corrections to the NR-calibration parameters $\delta\theta$, using different priors.

cient flexibility to match NRHybSur3dq8 with the required precision, for the same values of the physical parameters λ . This could be due to the ineffectiveness of the parameters being varied, missing physics in the SEOBNRv5HM model (e.g., some higher-order modes), or potential inaccuracies in the NRHybSur3dq8 model (either due to NR resolution or to the hybridization procedure), which may become significant at such high SNRs [33]. This is expected, as the chosen $\delta\theta$ may not fully account for all sources of error, and mismodeling in other parts of the waveform construction could become relevant at sufficiently high SNR.

One possible explanation for the residual biases is the absence or mismodeling of higher-order modes. To address this, we first perform a test where we include the same set of modes in both the injection and recovery waveform models. Specifically, NRHybSur3dq8 includes the $(\ell, m) = (2, 0), (3, 1), (3, 0), (4, 2), (5, 5)$ modes, which are not incorporated by default in SEOBNRv5HM. We find that this change reduces the biases only slightly, and does not qualitatively affect the results, indicating that the lack of higher-order modes is not the primary source of error.

In SEOBNRv5HM, higher-order modes are calibrated to NR in the merger-ringdown phase, but they are less accurate than the dominant $(2, 2)$ mode [28]. This is due to both the lower NR quality for these modes and the increased difficulty of fitting subdominant modes, which often exhibit complex morphologies. The $\delta\theta$ parameters we focus on do not account for these inaccuracies. To assess the impact of higher-mode mismod-

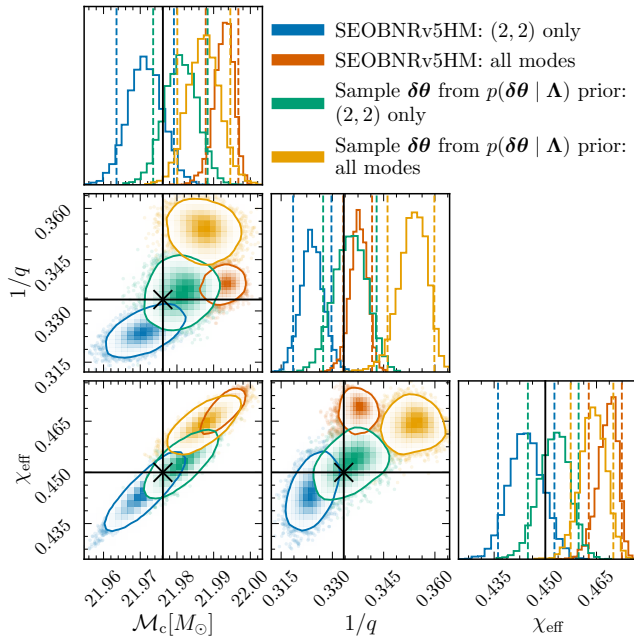


Figure 10. Marginalized posterior distributions for the chirp mass, inverse mass ratio, and effective spin in the ET-A# detector network. Parameter estimation is performed by injecting a NRHybSur3dq8 signal and recovering it using SEOBNRv5HM, either sampling only the standard source parameters, or including corrections to the NR-calibration parameters $\delta\theta$. For $\delta\theta$, both uniform priors and $p(\delta\theta | \Lambda)$ priors, reflecting NR-calibration uncertainty, are used. We compare results using all available modes in both the signal and template, and using only the dominant (2, 2) mode. In the latter case, biases are mitigated when sampling on $\delta\theta$.

eling, we repeat the analysis using only the dominant (2, 2) mode in both the signal and template. We show in Fig. 10 the marginalized posterior distributions for the chirp mass, inverse mass ratio, and effective spin. In this case, we observe that biases are still present in SEOBNRv5HM, but are mitigated when sampling on $\delta\theta$. This indicates that mismodeling of higher-order modes is a significant source of error. To address this, additional $\delta\theta$ parameters should be considered to account for mismodeling specific to higher-order modes. This could be achieved by introducing parameterized deviations in the amplitude and frequency at the merger, similar to what is done in tests of GR [138], after determining appropriate priors across the parameter space.

Impact of NR length on calibration

In this section, we investigate whether the NR calibration of SEOBNRv5 (and its associated uncertainty), which is only informative of the accuracy of the model at frequencies larger than the initial NR starting frequency for each simulation, is sufficient to constrain the low-frequency portion of the waveform, not covered by NR simulations. Since direct compari-

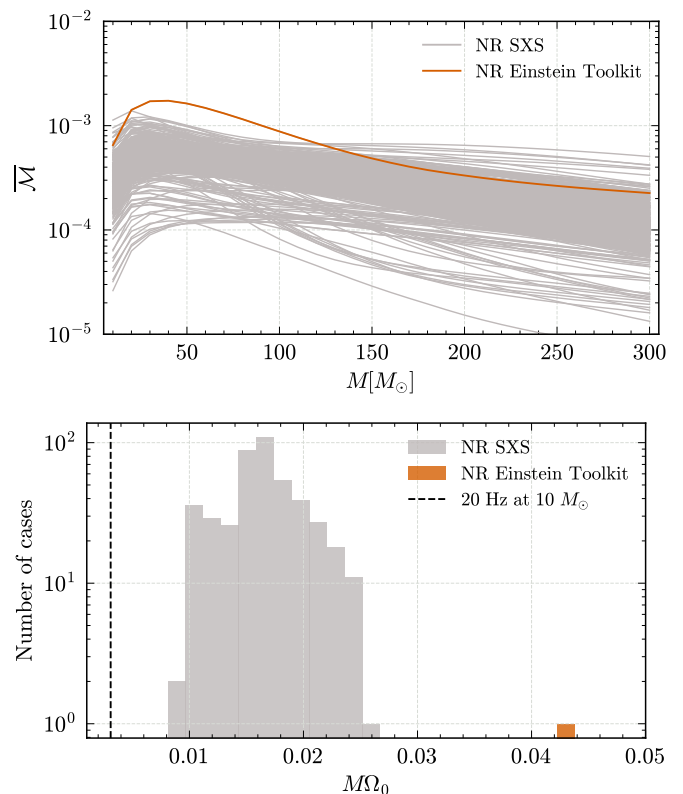


Figure 11. *Top panel:* median mismatch between SEOBNRv5 using for the calibration parameters θ the calibration posterior median, and SEOBNRv5 with 100 posterior samples, starting from a frequency of 20 Hz for $10M_\odot$. Each curve corresponds to the calibration posterior obtained from one of the 400 spinning NR simulations used in this work. *Bottom panel:* dimensionless initial frequency of the NR waveforms used in this work. We highlight in orange the $q = 8$ Einstein Toolkit simulation, which covers 7.4 orbits and is the shortest we employ. The black dashed line indicates the frequency at which we start the mismatch computation in this section.

son with NR is not possible in this regime, we perform internal consistency tests. Specifically, we assess if different values of the EOB calibration parameters θ that faithfully reproduce an NR waveform with parameters Λ at high frequencies (e.g., different calibration posterior samples from $p(\theta | \Lambda)$) can result in significant variations in the low-frequency behavior. To do so, we compute the unfaithfulness between SEOBNRv5 taking a reference value for the calibration parameters θ (e.g., the posterior median) and SEOBNRv5 using different posterior samples. We compute the average unfaithfulness $\bar{\mathcal{M}}$ over 100 samples for each NR case, starting from a frequency of 20 Hz for $10M_\odot$ (corresponding to a dimensionless frequency $M\Omega_0 \approx 0.003$), which is much lower than the typical NR starting frequency, as shown in the bottom panel of Fig. 11. This was previously investigated for the SEOBNRv4 model in Sec. 6 of Ref. [19] (see, e.g., Fig. 7), starting however at a larger frequency of 25 Hz for $20M_\odot$.

The top panel Fig. 11 shows the median mismatch as a function of the total mass. The unfaithfulness generally re-

mains below the 10^{-3} level, which is comparable to the mismatch against NR using different posterior samples in the high-frequency region. This means that different values of the calibration parameters do not significantly affect the low-frequency behavior, even for very short NR waveforms (e.g., the $q = 8$ Einstein Toolkit waveform covering only 7.4 orbits). This indicates that the low-frequency behavior of the model is robust, with most uncertainty arising from the late-inspiral and merger portions of the signal covered by NR. In contrast, for SEOBNRv4, the mismatch could exceed 10% for the $q = 8$ Einstein Toolkit simulation. The better behavior of SEOBNRv5 is likely due to having fewer calibration parameters compared to SEOBNRv4, which are only needed to correct the final portion of the waveform, thanks to a more

accurate analytic baseline model.

Posterior distributions

For completeness, we show in Figs. 12 and 13 the marginalized posterior distributions for the parameter recoveries of the configurations with $q = 3$ and $\chi_i = \pm 0.45$ across the different detector networks. This provides a complementary picture to Figs. 3 and 9, which focus only on biases in the 1D marginalized posteriors, by illustrating correlations between parameters and the appearance of biases in the 2D marginalized posteriors. This also serves to highlight the significant improvement in measurement precision with higher SNR signals seen by upcoming GW detectors.

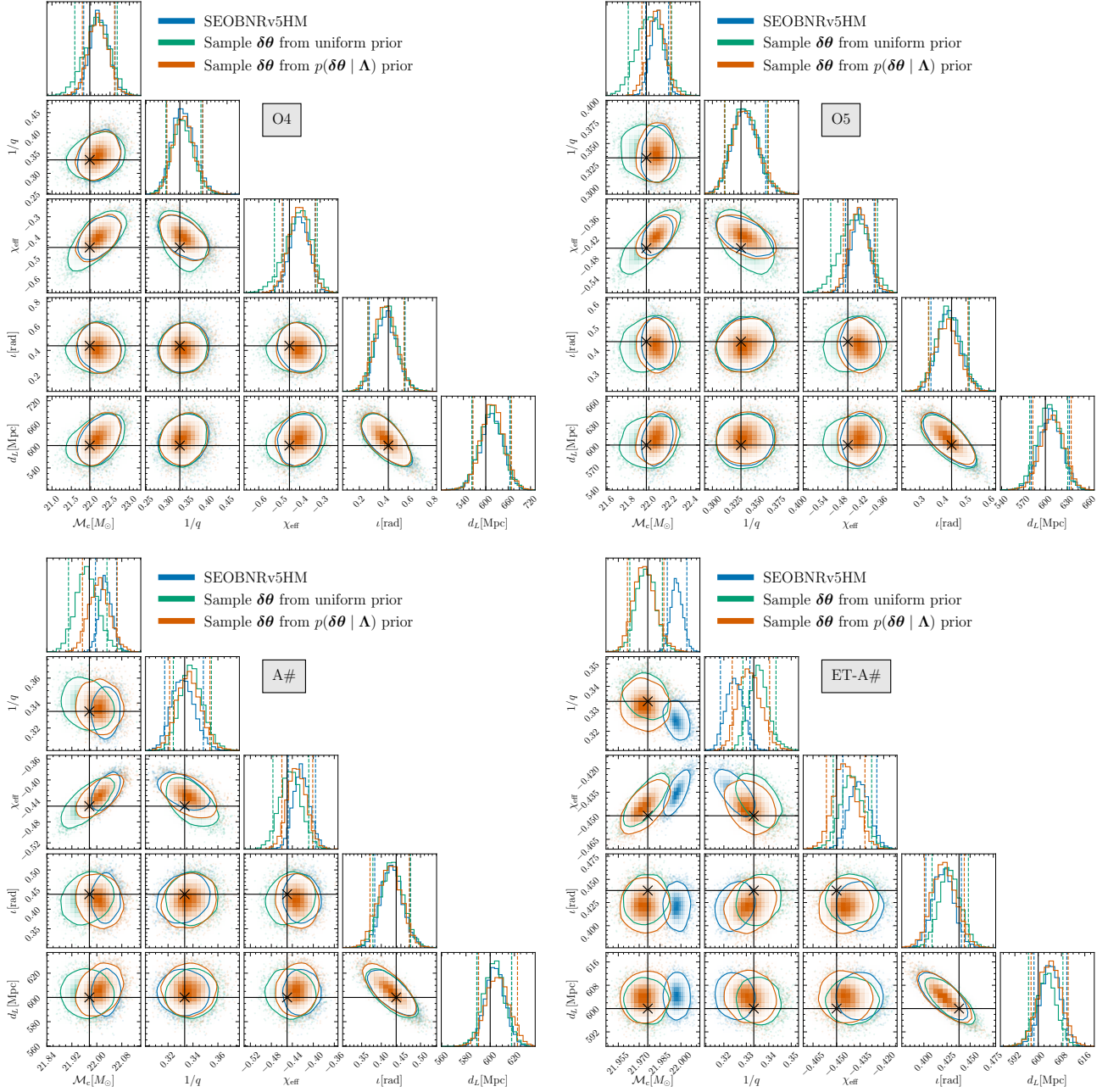


Figure 12. Marginalized posterior distributions for the chirp mass, inverse mass ratio, effective spin, inclination, and luminosity distance, in the different detector networks. Parameter estimation is performed by injecting a NRHybSur3dq8 signal, with unequal masses ($q = 3$) and negative spins ($\chi_1 = \chi_2 = -0.45$), and recovering it using three versions of SEOBNRv5HM: one sampling only the standard parameters, and the others including corrections to the NR-calibration parameters $\delta\theta$. For $\delta\theta$, both uniform priors and $p(\delta\theta | \Lambda)$ priors, reflecting NR-calibration uncertainty, are used.

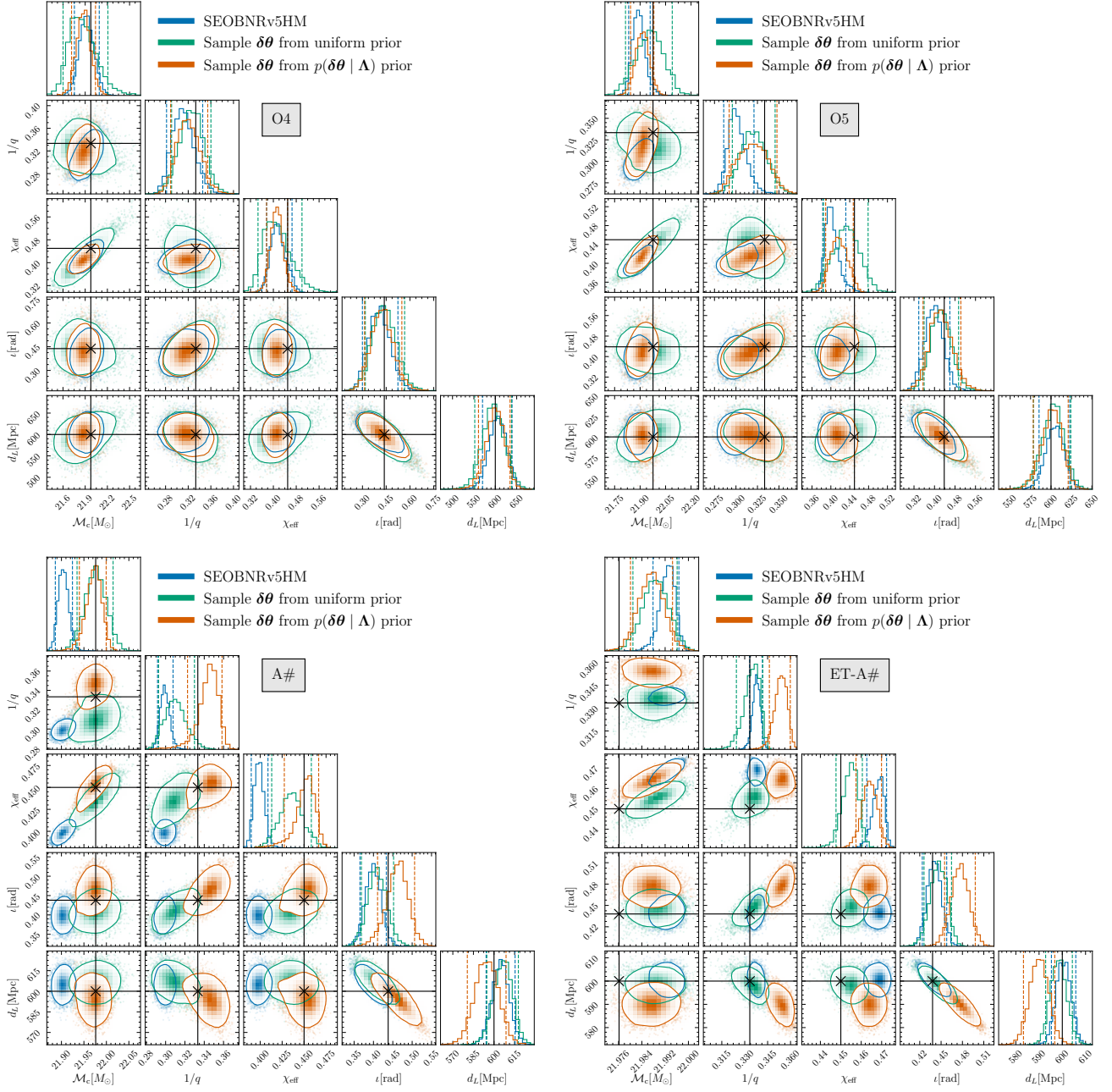


Figure 13. Marginalized posterior distributions for the chirp mass, inverse mass ratio, effective spin, inclination, and luminosity distance, in the different detector networks. Parameter estimation is performed by injecting a NRHybSur3dq8 signal, with unequal masses ($q = 3$) and positive spins ($\chi_1 = \chi_2 = 0.45$), and recovering it using three versions of SEOBNRv5HM: one sampling only the standard parameters, and the others including corrections to the NR-calibration parameters $\delta\theta$. For $\delta\theta$, both uniform priors and $p(\delta\theta | \Lambda)$ priors, reflecting NR-calibration uncertainty, are used.